Journal of Applied Fluid Mechanics, Vol. 18, No. 9, pp. 2297-2308, 2025.
Available online at www.jafmonline.net, ISSN 1735-3572, EISSN 1735-3645.
https://doi.org/10.47176/jafm.18.9.3399

Experimental and Numerical Study of Flow over Rectangular Cavity

A. Pinarbasi[1†], B. Yesilata[2], H. Akilli[3], C. Ozalp[4] and M. M. Aksoy[4]

[1] *Department of Mechanical Engineering, Ankara Yildirim Beyazit University, Turkey*
[2] *Department of Energy Systems Engineering, Ankara Yildirim Beyazit University, Turkey*
[3] *Department of Mechanical Engineering, Cukurova University, Turkey*
[4] *Department of Energy Systems Engineering, Osmaniye Korkut Ata University, Turkey*

†*Corresponding Author Email: apinarbasi@aybu.edu.tr*

ABSTRACT

This study investigates shear-thinning non-Newtonian fluid flow over a rectangular cavity using both experimental and numerical approaches. Small concentrations, varying between 0.25% and 1.0% of polyacrylamide (PAM) with high molecular weight, were used to form the non-Newtonian solution. In the experimental phase, Particle Image Velocimetry (PIV) was employed to obtain time-averaged velocity fields and recirculation characteristics. These experimental findings were compared with numerical simulations using Computational Fluid Dynamics (CFD) in which the fluid behavior was characterized using the Carreau rheological model. Excellent agreement was achieved between experimental and numerical results for velocity vectors, streamwise and transverse velocity contours, and vorticity distributions across Reynolds numbers ranging from 5 to 50. The structural flow changes within and in the vicinity of the rectangular cavity resulting from increasing Reynolds numbers are analyzed in detail, with particular emphasis on how the shear-thinning properties influence vortex formation, recirculation zones, and velocity gradients.

Article History

Received January 22, 2025
Revised April 7, 2025
Accepted April 11, 2025
Available online July 5, 2025

Keywords:

Particle Image Velocimetry
Shear-thinning non-Newtonian fluid
Cavity
Carreau model
Computational fluid dynamics

1. INTRODUCTION

Flow over cavities is a complex problem especially when fluid is not Newtonian. The complexities are due to the deviatoric stress field influenced by the polymeric effects. The stress field is coupled to the fluid kinematics and is a function of the integral history of local deformation rates subjected to a fluid element moving along closed streamlines. The existence of a viscoelastic fluid memory, shear thinning effects in material functions, difference in non-zero normal stress and the complex extensional rheological behavior of non-Newtonian fluids each influence the fluid kinematics in the cavity geometry (Pakdel & McKinley, 1998). Flow over cavities is investigated extensively because it is a geometry of significant importance for both academic research and industrial applications. Studies on flow over cavities are in general classified as open-channel flows, pressure driven flows and lid-driven flows.

Considering the cavity flow in open channels, it is a subject of considerable importance in various engineering applications like aircraft for military use, automobile sunroof or openings between train wagons, blood flow in arteries. Moreover, it has attracted considerable interest from researchers because it is a benchmark problem for separation flows in a finite area (Citro et al., 2015). This problem also receives attention of rheological community since pressure measurements are conducted by drilling a hole in the conduit where a pressure transducer is placed in the hole. In the context of viscoelastic fluids, this results in the 'pressure-hole error' (Mitsoulis et al., 2006).

Pressure driven flow over cavities of non-Newtonian fluids were investigated by few researchers. Citro et al. (2015) investigated stability problem of Carreau fluid flows over an open square cavity using linear theory with a normal-mode decomposition. Discretization of the governing equations was performed with a finite element method and stability maps were constructed as functions of Reynolds number as well as the model parameters of n and λ. Their results indicated that for steady flow, the first global linear instability was the existence of a steady or unsteady 3-D bifurcation affected by the power-law index of n. The instability mechanism always lies down within the cavity and the results of linear stability analysis suggest the existence of a strong relation with the well-known lid-driven cavity problem. Pressure driven flow of a Bingham plastic over a square cavity within a channel was studied numerically by Mitsoulis et al. (2006). In their study, the

Nomenclature			
CFD	Computational Fluid Dynamics	v	transverse velocity
D	cavity depth	w	vorticity
PAM	polyacrylamide	λ	time constant
PIV	Particle Image Velocity		
Re	Reynolds number	n	power-law index
u	streamwise velocity	η_0	zero-shear viscosity

scope and structure of yielded/unyielded areas were well represented when using a criterion of the magnitude of extra stress tensor exceeding the yield stress. Power law shear thinning fluid flow in a micro-channel was studied numerically by Hamedi and Rahimian (2011) to investigate blood flow in arteries. Velocity, shear stress and vorticity profiles were analyzed for inline, staggered, and trapezoid cavity shapes. It was found that the vorticities diminished for highly pseudo-plastic fluids.

Compared to pressure-driven flows and open channel flows, lid-driven cavity flow of non-Newtonian fluids is the most extensively studied subject in this field. It serves as a benchmark geometry because it encompasses a wide range of flow phenomena of interest, including recirculation, singularity, instability, and transient behavior. Moreover, it is a benchmark geometry for various polymer processing applications such as extrusion, injection molding, die casting, short-dwell, and flexible blade coaters, scraped surface heat exchangers for the processing of highly viscous food materials. Among many researchers, Pakdel and McKinley (1998) are considered pioneers in the study of lid driven cavity flow of viscoelastic fluids. Using various experimental methods, they examined two semi-dilute viscoelastic solutions. At low Deborah number (De), the flow is two-dimensional, whereas increasing values of the imposed velocity resulted in progressive shifting of the primary recirculating vortex center to the upstream. At large De numbers, the fluid motion became unstable due to the development of three-dimensional flow. At the onset conditions, the disturbances seen in spatially periodic flow cells form which moved along the central position of the cavity. In addition, they observed hydrodynamic instabilities which were driven inertially in the shape of secondary flow structure. Pakdel and McKinley (1997) later performed another experimental study for non-Newtonian flows in various complex geometries such as lid driven cavities and demonstrated effective utilization of kinematic measurements and capturing secondary flows. Sriram et al. (2008) studied transient periodic flow of viscoplastic fluids in a cuboidal cavity when top plate moves with periodic motion. In a similar experimental study, Grillet et al. (2000) investigated elastic instabilities in a lid-driven cavity for a Boger fluid. Their study indicated that for shallow cavity shapes, the polymer stress starting from the downstream corner of the cavity can reach the region of curved streamlines at the bottom of the cavity and this is likely to produce an elastic instability. Additionally, Anantha Kumar et al. (2018, 2019a) numerically investigated the flow of non-Newtonian fluids over stretched surfaces with magnetohydrodynamic (MHD) effects, with particular emphasis on heat transfer characteristics.

Numerical investigations of non-Newtonian fluid flow in lid-driven cavity geometries have employed diverse rheological models and computational techniques to capture the complex flow behaviors. These studies can be categorized according to the constitutive models used to characterize the non-Newtonian fluid behavior. For viscoplastic fluids, the Bingham model has been implemented through various numerical approaches, including the augmented Lagrangian method (Zhang, 2010), finite volume methods (Thohura et al., 2019; Syrakos et al., 2013), and finite element methods (Mitsoulis & Zisis, 2001). Additional viscoplastic formulations such as the Casson fluid model have been analyzed using the Runge–Kutta method (Anantha Kumar et al., 2019b, 2020). Shear-thinning fluids have frequently been represented using the Power-law model, solved via finite element methods (Sun et al., 2006; Aguirre et al., 2018), finite volume methods (Xu et al., 2018), and lattice Boltzmann approaches (Wang et al., 2016). Notable contributions to this category include the works of Mendu and Das (2012) and Chen and Shu (2019).

The Carreau and Carreau-Yasuda models, which more accurately capture the plateau regions at very low and high shear rates, have been implemented through various numerical frameworks. Shamekhi and Sadeghy (2009) employed the Point Interpolation Method, Anderson et al. (2000) utilized Spectral Element Methods, Kim and Reddy (2019) implemented mixed least-squares Finite Element Methods, and Haque et al. (2012) developed a second-order Finite Difference approach.

More complex viscoelastic fluid behavior has been addressed through sophisticated constitutive equations. The Upper Convected Maxwell model has been implemented in finite volume simulations (Fernandes et al., 2019), while the Oldroyd-B model has been studied using finite element methods (Baloch et al., 2002). Sousa et al. (2016) compared both Upper Convected Maxwell and Oldroyd-B models using a finite volume framework. For advanced polymer rheology, Varchanis et al. (2019) investigated the Oldroyd-B and Phan-Thien-Tanner (PTT) models using finite element methods, Grillet et al. (1999) implemented the CR-FENE dumbbell model with mixed finite element methods, and Santos et al. (2011) explored the SMD model using multi-field Galerkin least-squares approximations.

These diverse approaches highlight the rich variety of constitutive models and numerical techniques available for studying non-Newtonian fluid flow in cavity geometries, reflecting the complexity of accurately representing their rheological behavior.

A careful review and evaluation of the literature indicates an important gap in the fact that the studies of

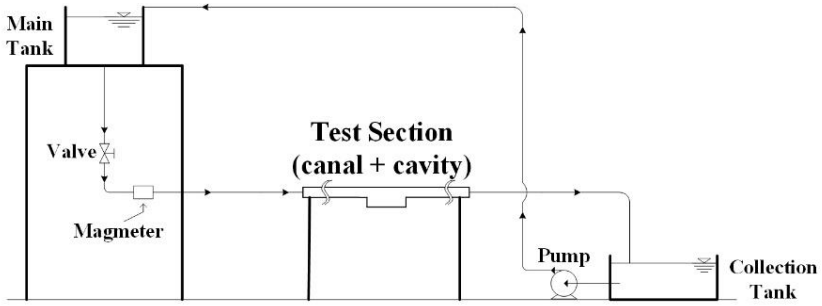

Fig. 1 Schematic of the experimental setup

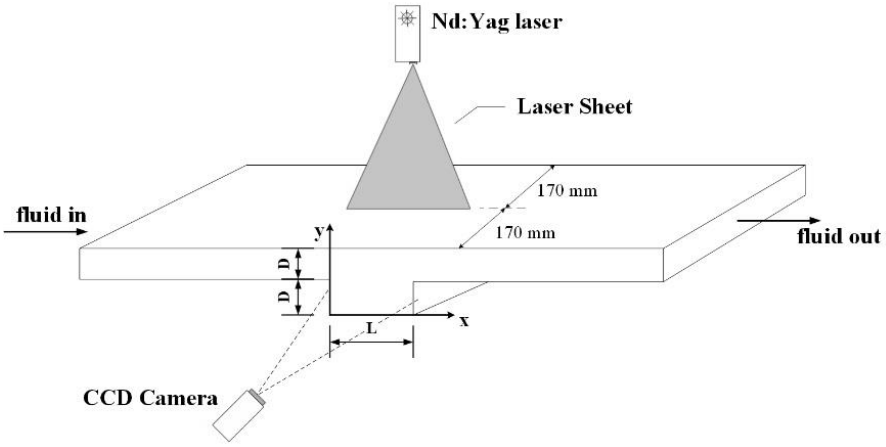

Fig. 2 Schematic of the test-section with representative illustrations of location, orientation of laser sheet and camera field of view

rheological model fluids in cavity flows have been predominantly numerical, with limited experimental validation. Therefore, this study addresses this gap by providing a comprehensive experimental investigation of shear-thinning non-Newtonian fluid flow over a rectangular cavity using polyacrylamide (PAM) solutions. Time-averaged velocities, streamlines and vortex characteristics are measured by using Particle Image Velocimetry (PIV) method. PIV is a powerful tool for measuring that can be utilized to attain time dependent full field velocity distributions for both single and multi-phase flows. Moreover, the experimental results are systematically compared with computational fluid dynamics (CFD) simulations using ANSYS Fluent, where the fluid behavior is characterized by the Carreau rheological model. This dual experimental-numerical approach reveals excellent agreement for velocity vectors, streamwise and transverse velocity contours, and vorticity distributions across Reynolds numbers ranging from 5 to 50. Our findings provide valuable insights into how the shear-thinning properties of PAM solution influence flow structures, recirculation patterns, and vorticity fields in rectangular cavity geometries, with implications for various industrial applications including polymer processing, pharmaceutical mixing, and coating operations.

2. MATERIAL AND METHOD

2.1. Experimental Setup

The test section containing the rectangular cavity used in this study is presented schematically in Fig. 1. In order to facilitate flow visualization, all test sections were constructed from plexiglas (acrylic) material. The cavity has an aspect ratio (L/D) of 2.0, with a length of L=60 mm and depth of D=30 mm. The test section consists of a main tank and a collection tank with appropriate fluid pumping components. The main tank is manufactured in a way that it has two separate containers as inner and outer ones. The fluid level in the inner small tank remains constant, with any overflow directed to the outer tank. The outer tank connects to the collection tank via a by-pass line, allowing excess fluid to transfer to the collection tank by free fall when the fluid level rises. Fluid drawn from the collection tank is pumped back to the inner tank, creating a closed circulation system.

A high-image-density PIV system was used in order to capture the flow behavior in the cavity and enable quantitative visualization of flow patterns. The placement and setup of the laser sheet are represented in Fig. 2. The PIV technique provides a global representation of the flow field in a quantitative manner. These unique capabilities allow for physical insights into the nature of these complex flows. Illumination of tracer particles in the PIV system is achieved using a 1-2 mm thick laser sheet produced by Nd:YAG pulsed lasers.

Lasers have 120 mJ power rating, equipped with a cylindrical lens system.

A magnetic flow meter was used to monitor the mass flow rate of fluid passing through the test section, enabling determination of average velocity and Reynolds number. The working fluid consisted of a 0.5% concentration by

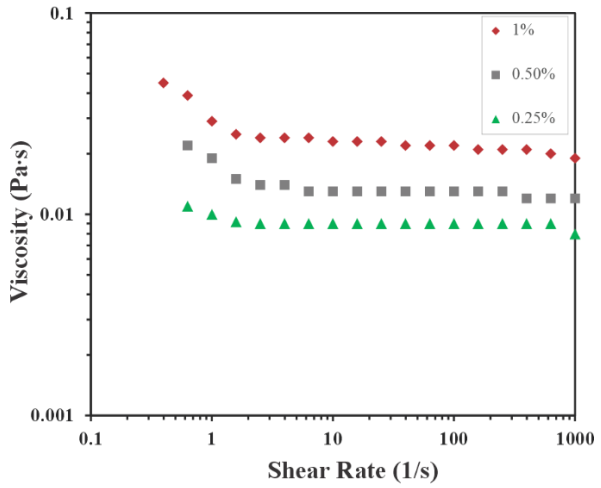

Fig. 3 Viscosity-shear rate curves of the polyacrylamide (PAM) polymer solutions

weight of high molecular weight polyacrylamide (PAM) in pure water, creating a shear-thinning non-Newtonian solution. The rheological properties of this fluid are measured by a rotational cone-plate rheometer (ARES-G2 Rheometer by TA Instruments). The viscosity-shear rate values at concentration ratios of 0.25%, 0.5% and 1% by weight are shown in Fig. 3. The viscosities of all three solutions exhibit moderate level of shear-thinning behavior primarily within the shear rate range of approximately 10-1s-1–101s-1. At higher shear rates, up to 103s-1, viscosities remain practically constant at a value close to the infinite shear viscosity. Due to more consistent infinite shear-rate viscosity behavior at higher shear rates, the PAM fluid with 0.5% concentration is utilized through all experiments in this study. The fluid parameters used in rheological model were determined from the shear stress - shear rate curves of the fluid at this concentration for shear rate ranges between 10-3s-1–105s-1 as presented in the next section (Section 2.2). During most of the flow conditions examined (Re = 5–50) here, the fluid experiences shear rates predominantly above 101s-1, where the viscosity remains practically constant at its lower (infinite shear-rate) limit. However, existences of localized regions with much lower shear rates within the stagnant and recirculation zones of the flow over the cavity cause in experiencing with the moderately higher viscosities, which is one of the challenges to be explored in this study.

When performing PIV experiments, metallic coated hollow plastic spheres with a diameter of 12 μm, which are essentially neutrally buoyant, were seeded into the fluid. The densities of metallic particles and fluid mixture used in experiments were 1100 kg/m^3 and 1020 kg/m^3, respectively, ensuring homogeneous movement of the particles with the fluid. PIV images were captured at a framing rate of 15 frames per second in cinema mode. A time sequence of 350 images was acquired for each experimental condition. A digital camera with a resolution of 1086×1016 pixels, makes possible the acquisition of the patterns of particle images in the flow. Experimental uncertainties of velocity measurements are found to be within 1%. More details about PIV method can be found in earlier study of us (Ozalp et al., 2010; Pinarbasi et al., 2015).

2.2. Numerical Framework

Since experimental studies of this study are conducted at atmospheric pressure and ambient temperature, only the continuity and momentum conservation equations were considered for numerical analysis, eliminating the need for the energy equation terms. The governing equations for incompressible flow are presented below.

Continuity equation:

$$\nabla \cdot u = 0 \tag{1}$$

Momentum conservation equation:

$$\rho(u \cdot \nabla)u = -\nabla p + \nabla \cdot \tau \tag{2}$$

where τ is the stress tensor related to the viscosity through:

$$\tau = \eta(\nabla u + \nabla u^T) \tag{3}$$

For the non-Newtonian fluid, the viscosity is a function of shear rate and is modeled using the Carreau rheological model:

$$\eta = \eta_\infty + (\eta_0 - \eta_\infty)(1 + \lambda^2\gamma^2)^{\frac{n-1}{2}} \tag{4}$$

The equations were solved under steady-flow conditions with atmospheric pressure of 101 kPa and without gravity terms. The numerical simulations were performed using ANSYS Fluent, a commercial computational fluid dynamics (CFD) software based on the finite volume method. The governing equations were discretized using a second-order upwind scheme for the convective terms, and the SIMPLE (Semi-Implicit Method for Pressure-Linked Equations) algorithm was employed for pressure-velocity coupling. For boundary conditions, velocity inlet with uniform profiles corresponding to each Reynolds number was specified at the inlet. A pressure outlet condition (atmospheric) was applied at the exit. All solid surfaces, including the top and bottom walls of the main channel as well as all cavity walls, were modeled as stationary surfaces with no-slip wall conditions. The fluid properties were defined using a user-defined database with a density of 1020 kg/m^3, and the rheological behavior was characterized using the Carreau constitutive equation as defined in Eq. (4). The solution was initialized using the inlet conditions to facilitate faster convergence. Steady-state simulations were performed for each Reynolds number case (Re = 5 to 50), and convergence was determined when the scaled residuals fell below 10^{-6} for all equations.

For all the results given in this study, the Carreau model parameters were kept constant with time constant λ (s) = 5, the power law index n = 0.5, the zero-shear viscosity η_0 = 0.022 Pa·s, and the infinite shear viscosity η_∞ = 0.012 Pa·s. These parameters were determined from rheological measurements of the PAM solution at 0.5% concentration. Figure 4 depicts the viscosity versus shear rate relationship for both the Carreau model and the experimental measurements at 0.5% PAM concentration, while Table 1 shows the comparison between measured viscosity values and those predicted by the Carreau model.

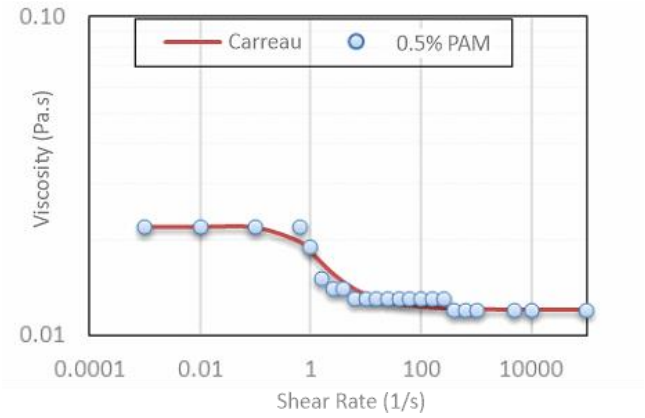

Fig. 4 Viscosity of Carreau model with respect to 0.5% concentration of PAM

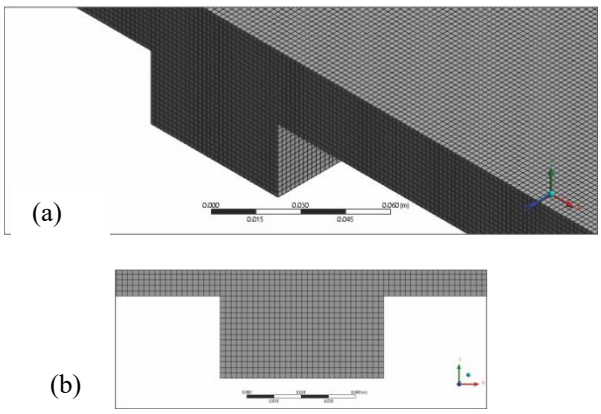

Fig. 5 Grid structure for numerical solution: (a) isometric view, (b) cavity front view

Table 1 Measured viscosity and Carreau model viscosity results at different shear rates

Shear Rate (1/s)	Viscosity (Pa·s)	Carreau viscosity (Pa·s)
0.001	0.022	0.022
0.01	0.022	0.020
0.1	0.022	0.020
0.631	0.022	0.020
1	0.019	0.018
1.585	0.015	0.017
2.512	0.014	0.016
3.981	0.014	0.015
6.31	0.013	0.014
10	0.013	0.013
15.849	0.013	0.013
25.119	0.013	0.013
39.811	0.013	0.013
63.096	0.013	0.012
100	0.013	0.012
158.49	0.013	0.012
251.19	0.013	0.012
398.11	0.012	0.012
630.96	0.012	0.012
1000	0.012	0.012
5000	0.012	0.012
10000	0.012	0.012
100000	0.012	0.012

The agreement is nearly perfect, especially at higher shear rates.

The mesh structure used for the quadrilateral cavity is shown in Fig. 5. A comprehensive grid independence study was conducted to ensure numerical accuracy. Three different mesh resolutions with 215,000 (coarse), 435,000 (medium), and 1,000,000 (refined) nodes were tested for grid independence. The velocity profiles along section B-B for Re = 50 were compared for both the streamwise (u) and transverse (v) velocity components, as shown in Fig.

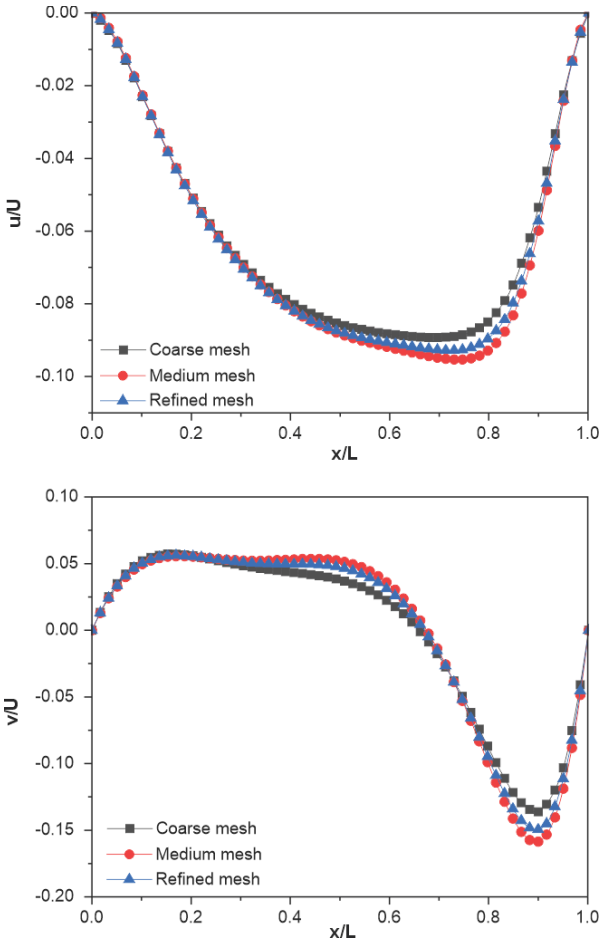

Fig. 6 Dependence of the numerical solution on computational grid for *Re*=50 for dimensionless streamwise (*u*/*U*) and transverse (*v*/*U*) velocity profiles along the line at position *D*/2 from bottom of the cavity

6. As evident from the figure, the results obtained with 435,000 and 1,000,000 nodes show negligible differences, with variations less than 2% in maximum velocity magnitude. Since the medium mesh results adequately capture the relevant fluid physics phenomena, we have employed the 435,000 node mesh for all subsequent simulations, providing an optimal balance between computational efficiency and solution accuracy.

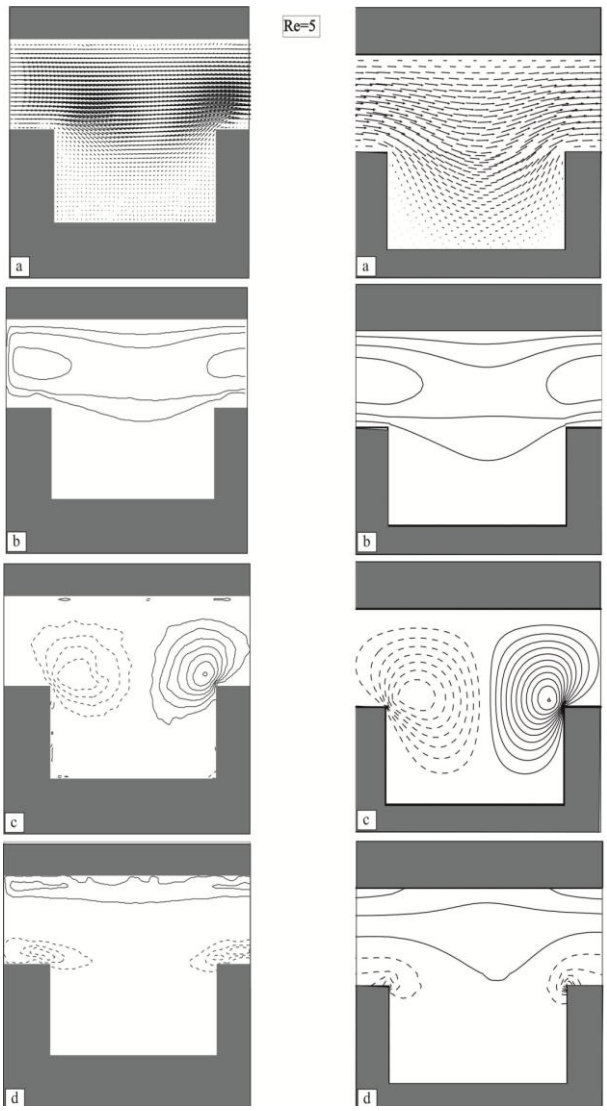

Fig. 7 Comparison of experimental (left column) and CFD (right column) results for *Re*=5

a) velocity vectors, b) streamwise velocity (u), c) transverse velocity (v), d) vorticity (w).

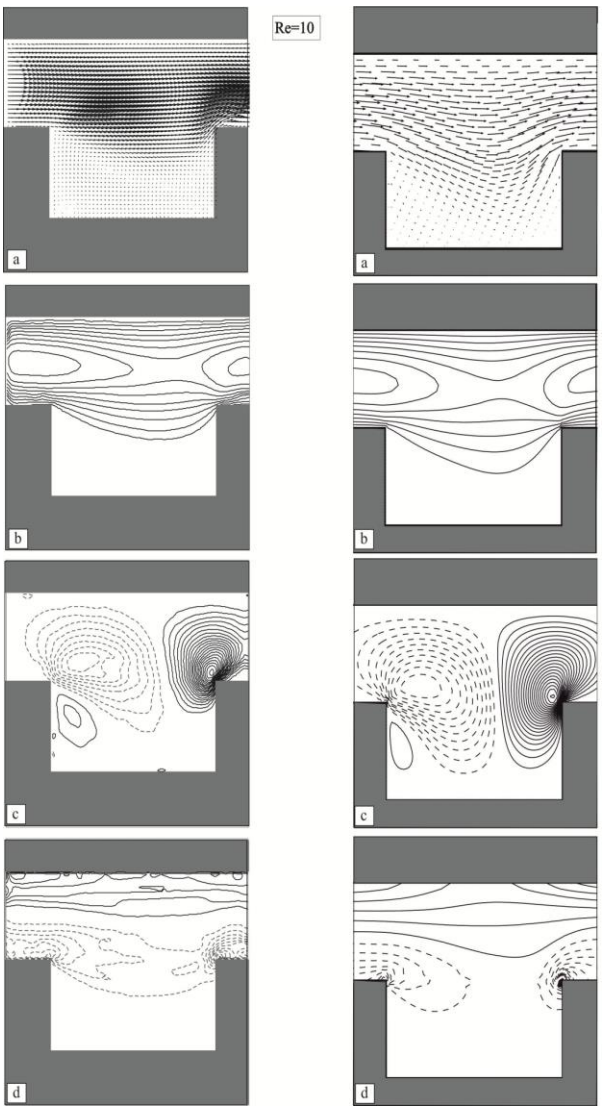

Fig. 8 Comparison of experimental (left column) and CFD (right column) results for *Re*=10. a) velocity vectors, b) streamwise velocity (u), c) transverse velocity (v), d) vorticity (w)

3. RESULTS AND DISCUSSION

Shear-thinning non-Newtonian fluid flow past a rectangular cavity was examined both experimental and numerical approaches. PIV measurements and CFD simulations were conducted across Reynolds numbers ranging from 5 to 50. Due to the predominantly shear-thinning behavior of the PAM solution used in this study, dimensional analysis focused on Reynolds number (Re) as the primary parameter, rather than Deborah or Weissenberg numbers which would be more relevant for highly elastic fluids.

We have presented a systematic comparison between experimental and numerical results comparatively in Figs. 7-12 for increasing values of *Re*, in the form of that the left column shows experimental results whereas the right column shows numerical results. For proper interpretation of experimental and numerical results, it is also important to note the range and increments of the measured variables: streamwise velocity (u_{min}=0.00095 m/s, u_{max}=0.00489 m/s, Δu=0.0015 m/s), transverse velocity (v_{min}=-0.00098m/s, v_{max}=0.00142m/s, Δv=0.0002 m/s), and vorticity (w_{min}= -1.16 s^{-1} , w_{max}= 0.74 s^{-1} , Δw=0.3 s^{-1}).

The velocity vector fields (first row in Figs. 7-12) reveal the progressive development of recirculation patterns as Reynolds number increases. At low Re values (5-10), the flow barely penetrates the cavity, with minimal circulation evident. As Re increases to 20 and beyond, the flow penetrates deeper into the cavity, and a well-defined recirculation zone forms. This behavior reflects how the balance between inertial and viscous forces shifts with the increasing Reynolds number. For the shear-thinning fluid, this effect is particularly pronounced because the local viscosity decreases in regions of high shear rate, enhancing momentum transfer into the cavity compared to what would be observed with a Newtonian fluid at equivalent Reynolds numbers (Ozalp et al., 2010).

The streamwise velocity (<u>) contours (second row in Figs. 7-12) demonstrate significant structural changes

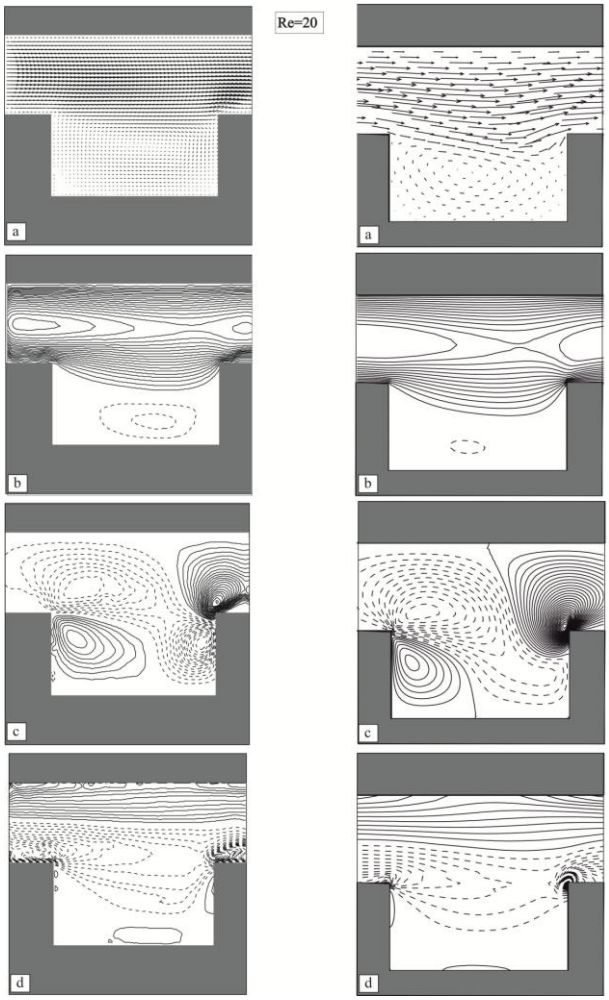

Fig. 9 Comparison of experimental (left column) and CFD (right column) results for *Re*=20. a) velocity vectors, b) streamwise velocity (*u*), c) transverse velocity (*v*), d) vorticity (*w*)

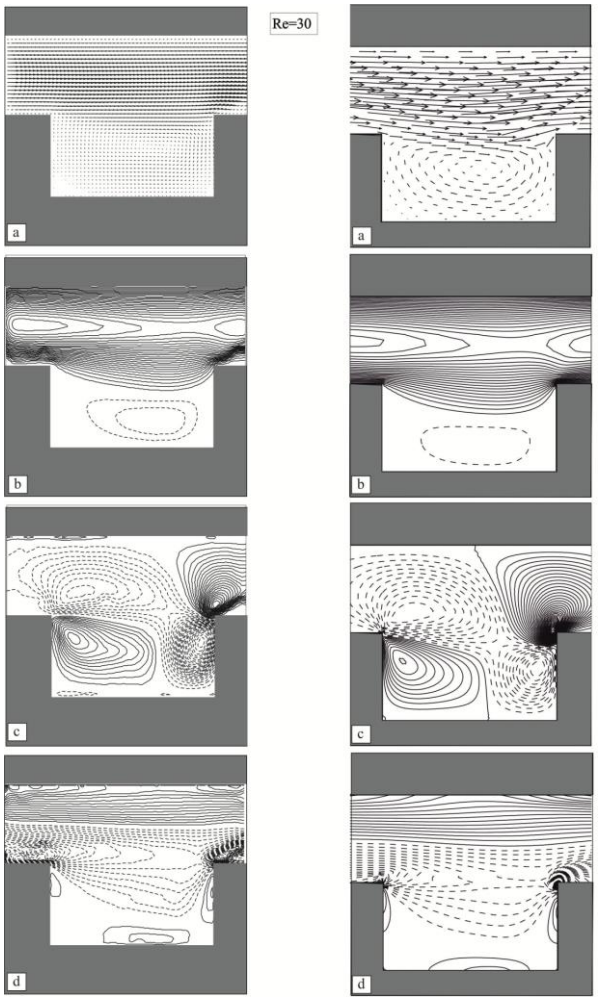

Fig. 10 Comparison of experimental (left column) and CFD (right column) results for *Re*=30. a) velocity vectors, b) streamwise velocity (*u*), c) transverse velocity (*v*), d) vorticity (*w*)

with increasing Reynolds number. Continuous lines represent positive (counterclockwise) velocities, while dashed lines indicate negative (clockwise) velocities. At Re=5 and Re=10, positive velocities dominate the upper region of the cavity, with no negative velocities present (Figs. 7 and 8). As Re increases to 20 and beyond, negative velocity regions emerge near the cavity center and progressively expand to occupy most of the lower cavity region at Re=50 (Figs. 9 through 12).

This evolution reflects the development of a coherent recirculation zone within the cavity. The distinct separation between positive velocities in the upper half and negative velocities in the lower half of the cavity becomes more pronounced at higher Reynolds numbers. This behavior is directly influenced by the shear-thinning properties of the fluid, as regions of high shear rate experience reduced viscosity, facilitating the formation and strengthening of recirculation patterns.

The transverse velocity (<*v*>) contours (third row in Figs. 7-12) exhibit a complex evolution with increasing Reynolds number. At Re=5 and Re=10, positive velocity contours appear primarily at the cavity exit, while negative contours dominate the entrance zone. As Re increases to 20 and beyond, a positive velocity region develops within the cavity near the entrance and progressively extends toward the exit wall. Concurrently, a negative velocity region forms within the cavity near the exit wall.

At Re=50, two distinct positive transverse velocity regions dominate: one extending from the entrance wall toward the exit wall within the cavity, and another at the exit region above the cavity. The negative velocity region occupies approximately half the area of the positive region within the cavity.

Shamekhi and Sadeghy (2009) reported similar trends in their numerical study of Carreau-Yasuda fluids, albeit at higher Reynolds numbers (400-1000). Their findings corroborate our observations regarding the increasing magnitude of streamwise velocity in the lower half of the cavity and increasing transverse velocity magnitudes at both lateral walls as Reynolds number increases. This agreement with previous literature validates our experimental and numerical approaches while confirming that these flow features are characteristic of shear-thinning fluids in cavity geometries.

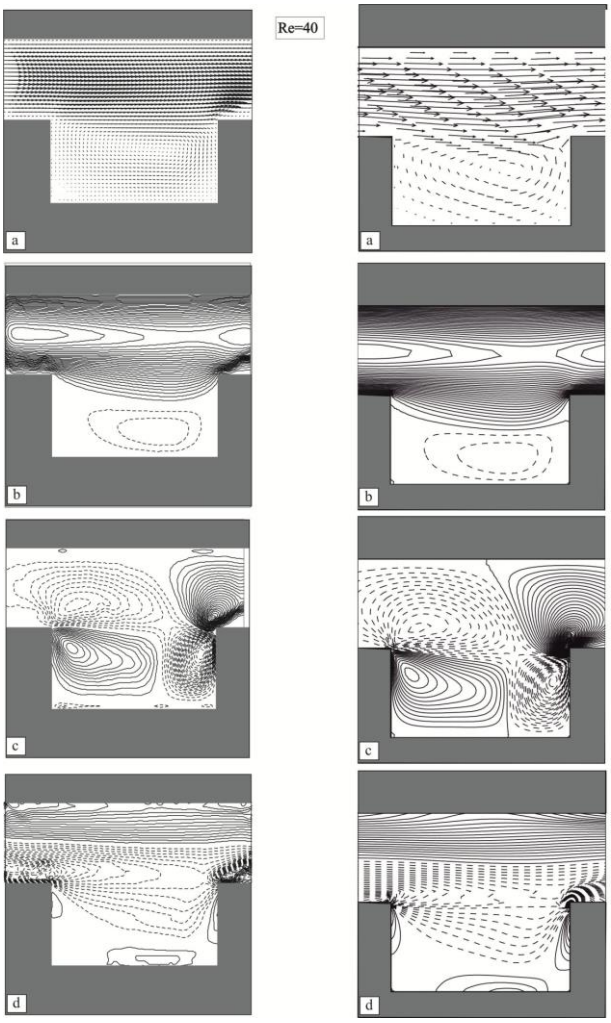

Fig. 11 Comparison of experimental (left column) and CFD (right column) results for *Re*=40. a) velocity vectors, b) streamwise velocity (*u*), c) transverse velocity (*v*), d) vorticity (*w*)

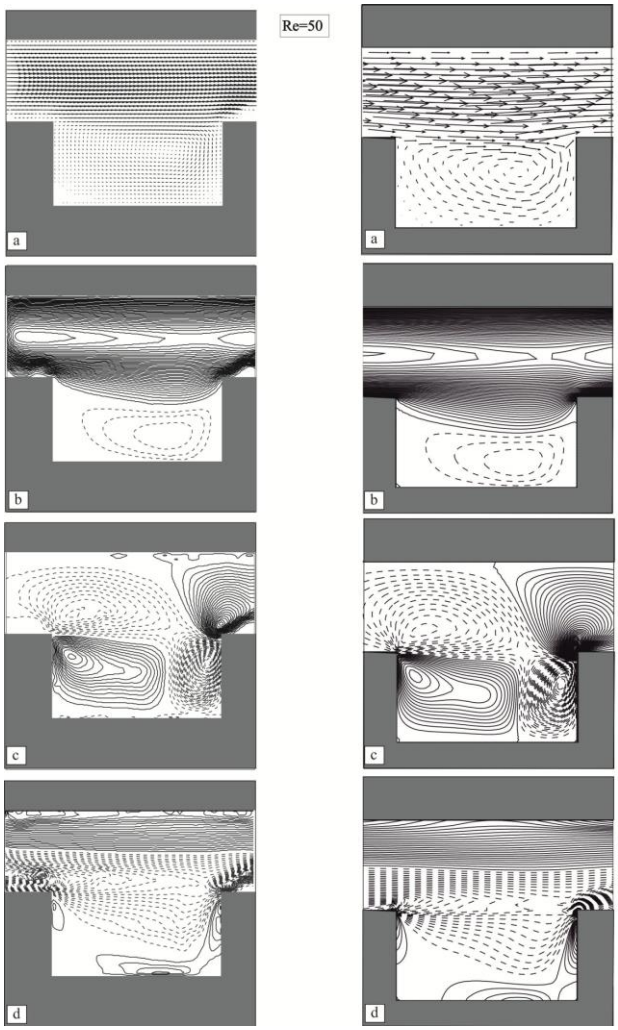

Fig. 12 Comparison of experimental (left column) and CFD (right column) results for *Re*=50. a) velocity vectors, b) streamwise velocity (*u*), c) transverse velocity (*v*), d) vorticity (*w*)

The vorticity contours (fourth row in Figs. 7-12) provide critical insights into the rotational characteristics of the flow. At Re=5 and Re=10, two small-scale negative vorticity regions form at the cavity entrance and exit. As Reynolds number increases, these negative vorticity regions penetrate deeper into the cavity and eventually merge, while a positive vorticity structure emerges in the lower cavity region.

A significant finding is that the onset of well-defined recirculation zones occurs at Re=20. Above this threshold, these structures persist and strengthen with increasing Reynolds number. At higher Re values (30-50), the negative vorticity regions shift toward the center and right portions of the cavity, while positive vorticity from the lower cavity region extends toward the exit.

The amplification of disturbances in the shear layer becomes more pronounced at higher Reynolds numbers, consistent with observations by Haque et al. (2012). They noted that the highest shear regions become more localized near walls while base-flow vorticity weakens toward the center and left side of the cavity. The formation of negative vortices at the upstream and downstream corners at low Reynolds numbers has also been observed by Yesilata et al. (1999), who described these as "lip vortices" – early indicators of flow instabilities arising from sudden changes in local shear rate. For shear-thinning fluids like the PAM solution used in this study, these structures are particularly significant as they reflect the rapid changes in local viscosity that occur in response to varying shear rates.

Moreover, with increasing Reynolds number, the detected secondary flows (particularly regions of positive vorticity) likely generate higher pressure gradients inside the cavity. While these enhanced flow structures would promote better cavity filling and more intense mixing –beneficial in processes such as injection molding – the associated pressure drops represent significant drawbacks that must be considered from a practical engineering perspective when dealing with shear-thinning fluids in such geometries.

Our overall observation from these results is that strong interplay between local viscosity variation versus local shear rate significantly impact the dynamic

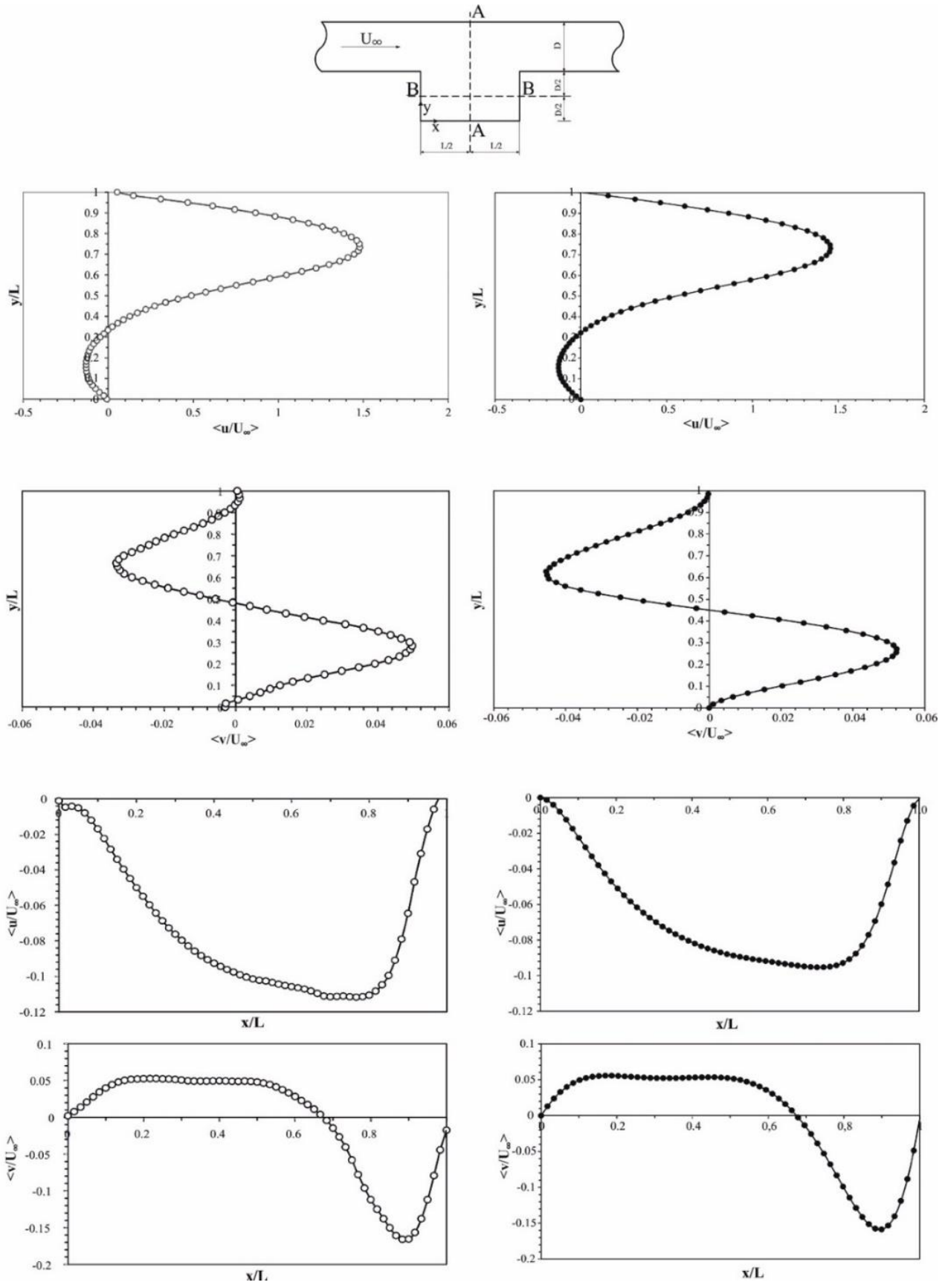

Fig. 13 Experimental (left column) and numerical (right column) streamwise (u/U) and transverse (v/U) velocity profiles at sections A-A (top four figures) and B-B (bottom four figures) for *Re* = 50

characteristics of flow over the rectangular cavity as follows. At low Reynolds numbers (Re ≤ 10), the fluid viscosity remains relatively high and uniform, limiting fluid penetration into the cavity. However, as Re increases

to Re = 20, shear-thinning effects become pronounced, leading to noticeable viscosity gradients and resulting in enhanced fluid penetration into the cavity. These gradients induce asymmetries in velocity profiles and amplify vortex strength and size due to the intensified momentum transfer into regions experiencing lower viscosity. Such behavior is consistent with previous observations in the literature for shear-thinning fluids (Shamekhi & Sadeghy 2009; Haque et al. 2012), which demonstrate how local viscosity reductions significantly influence the spatial distribution of vorticity and recirculation intensity within cavity geometries. It is also an emerging signal for evolutions of more distinct recirculation zones and vortex structures as we observe that these distinct secondary flow structures, including lip vortices at cavity corners, become more pronounced when *Re* further increases ($30 < \mathrm{Re} \geq 50$). The decreasing local fluid viscosities at high-shear rate regions result in significantly enhanced fluid mixing and intensified vortex formations as aforementioned above.

Figure 13 presents a detailed quantitative comparison between experimental and numerical results for dimensionless velocity profiles at two critical cross-sections: section A-A (traversing the cavity mid-point in the transverse direction) and section B-B (traversing the cavity mid-point in the streamwise direction). The results for Re=50 demonstrate excellent agreement between experimental measurements and numerical predictions at both locations, further validating the accuracy of our numerical model.

The velocity profiles at these sections provide additional insights into the flow structure not immediately apparent from the contour plots. The streamwise velocity profile at section A-A exhibits a characteristic S-shaped curve, with positive values in the upper region transitioning to negative values in the lower region, confirming the presence of a well-developed recirculation zone. The transverse velocity profiles show complex patterns that reflect the three-dimensional nature of the flow within the cavity.

This quantitative agreement between experimental and numerical approaches across multiple visualization methods (vectors, contours, and profiles) demonstrates the robustness of our findings and establishes a solid foundation for understanding the fundamental physics governing shear-thinning fluid behavior in rectangular cavity geometries.

4. CONCLUDING REMARKS

This study investigated shear-thinning non-Newtonian fluid flow over a rectangular cavity using complementary experimental and numerical approaches. A 0.5% concentration by weight of high molecular weight polyacrylamide (PAM) was used to create the shear-thinning solution. In the experimental phase, Particle Image Velocimetry (PIV) provided detailed measurements of time-averaged statistics. For the numerical simulations, the Carreau rheological model was implemented in ANSYS Fluent to characterize the fluid's complex behavior.

A systematic comparison between experimental and numerical results was conducted for Reynolds numbers ranging from 5 to 50, examining velocity vectors, streamwise and transverse velocity contours, and vorticity distributions. The excellent agreement between experimental and numerical results validates both approaches and provides confidence in the observed flow physics.

Moreover, as Reynolds number increased, the main flow progressively penetrated deeper into the cavity, generating stronger circulation patterns. The flow developed a distinctive structure featuring positive velocity regions in the upper half and negative velocity regions in the lower half of the cavity. Dual positive transverse velocity zones emerged; one extending from the entrance wall toward the exit wall within the cavity, and another at the exit region above the cavity. The highest shear stress regions became increasingly localized near the cavity walls, while the base-flow vorticity weakened toward the center and upstream side of the cavity. Furthermore, the boundary layer thickness exhibited exponential growth with the increasing Reynolds number.

A particularly significant finding was the emergence of lip vortices at the sharp corners of the cavity at Re=20 and above. These structures form due to sudden changes in local shear rate, which are amplified in shear-thinning fluids due to the viscosity's dependence on shear rate. These lip vortices represent early indicators of potential flow instabilities that would likely intensify at Reynolds numbers beyond those examined in this study.

The detailed flow characterization provided by this study enhances our understanding of how shear-thinning rheology influences flow patterns in geometries with sudden expansions, with practical implications for numerous industrial applications including polymer processing, pharmaceutical mixing operations, and coating processes. Future work could extend this analysis to higher Reynolds numbers to examine the transition to time-dependent flow regimes and investigate the effects of different cavity aspect ratios on the observed flow phenomena.

Although this study focused on the shear-thinning aspects of the PAM solution using the Carreau model, it should be noted that these solutions can typically demonstrate viscoelastic properties that were not accounted in the current rheological framework since extremely low-weight concentration of polyacrylamide (= 0.5%) was used in our study. Future investigations can employ viscoelastic models such as the Phan-Thien–Tanner (PTT) model to provide a more comprehensive description of both shear-thinning and elastic effects, particularly for applications where elastic properties significantly influence flow dynamics.

ACKNOWLEDGEMENT

This study was supported by TUBITAK (Scientific and Technological Research Council of Turkey) through project number 110M033.

CONFLICT OF INTEREST

The authors wish to confirm that there are no known conflicts of interest associated with this publication.

AUTHORS CONTRIBUTIONS

Ahmet Pinarbasi: Conceptualization, validation, formal analysis, investigation, resources, writing original draft preparation, writing-review and editing. **Bulent Yesilata:** Conceptualization, validation, formal analysis, investigation, software, data curation, editing. **Muhammed Murat Aksoy:** Experimental analysis, CFD analysis, investigation, visualization. **Coskun Ozalp:** Conceptualization, validation, formal analysis, software, experiments, reviewing and editing, visualization. **Huseyin Akilli:** Conceptualization, validation, formal analysis, investigation, experimental analysis

REFERENCES

Aguirre, A., Castillo, E., Cruchaga, M., Codina, R., & Baiges, J. (2018). Stationary and time-dependent numerical approximation of the lid-driven cavity problem for power-law fluid flows at high Reynolds numbers using a stabilized finite element formulation of the VMS type. *Journal of Non-Newtonian Fluid Mechanics 257*, 22-43. https://doi.org/10.1016/j.jnnfm.2018.03.014

Anantha Kumar, K., Sugunamma, V., & Sandeep, N. (2018). Impact of Non-linear Radiation on MHD Non-aligned Stagnation Point Flow of Micropolar Fluid Over a Convective Surface. *Journal of Non-Equilibrium Thermodynamics*, *43*(4), 327–345. https://doi.org/10.1515/jnet-2018-0022

Anantha Kumar, K., Sugunamma, V., & Sandeep, N. (2019a). Numerical exploration of MHD radiative micropolar liquid flow driven by stretching sheet with primary slip: A comparative study. *Journal of Non-Equilibrium Thermodynamics*, *44*(2), 101–122. https://doi.org/10.1515/jnet-2018-0069

Anantha Kumar, K., Sugunamma, V., & Sandeep, N. (2020). Effect of thermal radiation on MHD Casson fluid flow over an exponentially stretching curved sheet. *Journal of Thermal Analysis and Calorimetry*, *140*(5), 2377–2385. https://doi.org/10.1007/s10973-019-08977-0

Anantha Kumar, K., Sugunamma, V., Sandeep, N., & Reddy, J. V. R. (2019b). MHD stagnation point flow of Williamson and Casson fluids past an extended cylinder: A new heat flux model. *SN Applied Sciences*, *1*(7), 705. https://doi.org/10.1007/s42452-019-0743-6

Anderson, P. D., Galaktionov, O. S., Peters, G.W.M., van de Vosse, F. N., & Meijer, H. E. H. (2000). Mixing of non-Newtonian fluids in time-periodic cavity flows. *Journal of Non-Newtonian Fluid Mechanics 93*, 265-286. https://doi.org/10.1016/S0377-0257(00)00120-8

Baloch, A., Grant, P. W., & Webster, M. F. (2002). Homogenous and heterogeneous distributed cluster processing for two- and three-dimensional viscoelastic flows. *International Journal for Numerical Methods in Fluids, 40*, 1347-1363. https://doi.org/10.1002/fld.368

Chen, Z., & Shu, C. (2019). Simplified lattice Boltzmann method for non-Newtonian power-law fluid flows. *International Journal for Numerical Methods in Fluids,* 1-17. https://doi.org/10.1002/fld.4771

Citro, V., Giannetti, F., & Pralits, J. O. (2015). Three-dimensional stability, receptivity and sensitivity of non-Newtonian flows inside open cavities. *Fluid Dynamics Research, 47,* 015503. https://doi.org/10.1088/0169-5983/47/1/015503

Fernandes, C., Vukcevic, V., Uroic, T., Simoes, R., Carneiro, O. S., Jasak, H., & Nobrega, J. M., (2019). A coupled finite volume flow solver for the solution of incompressible viscoelastic flows. *Journal of Non-Newtonian Fluid Mechanics, 265*, 99-115. https://doi.org/10.1016/j.jnnfm.2019.01.006

Grillet, A. M., Shaqfeh, E. S. G., & Khomami, B. (2000). Observations of elastic instabilities in lid-driven cavity flow. *Journal of Non-Newtonian Fluid Mechanics, 94*, 15-35. https://doi.org/10.1016/S0377-0257(00)00123-3

Grillet, A. M., Yang, B., Khomami, B., & Shaqfeh, E. S. G. (1999). Modeling of viscoelastic lid driven cavity flow using finite element simulations. *Journal of Non-Newtonian Fluid Mechanics*, *88*, 99-131.

Hamedi, H., & Rahimian, M. H. (2011). Numerical simulation of non-Newtonian pseudo-plastic fluid in a micro-channel using the Lattice Boltzman Method. *World Journal of Mechanics*, 231-242. https://doi.org/10.4236/wjm.2011.15029

Haque, S., Lashgari, I., Giannetti, F., & Brandt, L., (2012). Stability of fluids with shear-dependent viscosity in the lid-driven cavity. *Journal of Non-Newtonian Fluid Mechanics, 173-174,* 49-61. https://doi.org/10.1016/j.jnnfm.2012.02.004

Kim, N., & Reddy, J. N., (2012). 3-D least squares finite element analysis of flows of generalized Newtonian fluids. *Journal of Non-Newtonian Fluid Mechanics, 266*, 143-159. https://doi.org/10.1016/j.jnnfm.2019.03.004

Mendu, S. S., & Das, P. K. (2012). Flow of power-law fluids in a cavity driven by the motion of two facing lids – A simulation by lattice Boltzmann method. *Journal of Non-Newtonian Fluid Mechanics, 175-176,* 10-24. https://doi.org/10.1016/j.jnnfm.2012.03.007

Mitsoulis, E., & Zisis, T. (2001). Flow of Bingham plastics in a lid-driven square cavity. *Journal of Non-Newtonian Fluid Mechanics, 101*, 173-180. https://doi.org/10.1016/S0377-0257(01)00147-1

Mitsoulis, E., Marangoudakis, S., & Spyratos, M., Zisis, T., & Malamataris, N. A. (2006). Pressure

drivenflows of Bingham plastics over a square cavity. *Journal of Fluids Engineering, 128*, 993-1003. https://doi.org/10.1115/1.2236130

Ozalp, C., Pinarbasi, A., & Sahin, B., (2010). Experimental measurement of flow past cavities of different shapes. *Experimental Thermal and Fluid Science, 34,* 505-515. https://doi.org/10.1016/j.expthermflusci.2009.11.003

Pakdel, P., & McKinley, G. M. (1997). Digital particle image velocimetry of viscoelastic fluids, *AIChE Journal 43*, (2), 289-302. https://doi.org/10.1002/aic.690430202

Pakdel, P., & McKinley, G. M. (1998). Cavity flows of elastic liquids: purely elastic instabilities. *Physics of Fluids, 10* (5), 1058-1070. https://doi.org/10.1063/1.869631

Pinarbasi, A., Pinar, E., Akilli, H., & İnce, E. (2015). Shallow water experiments of flow past two identical square cylinders in tandem. *European Journal of Mechanics B/Fluids, 49,* 100-107. https://doi.org/10.1016/j.euromechflu.2014.08.009

Santos, D. D., Frey, S., Naccache, M. F., & Mendes, P. R. (2011). Numerical approximations for flow of viscoplastic fluids in a lid-driven cavity. *Journal of Non-Newtonian Fluid Mechanics, 166*, 667-679. https://doi.org/10.1016/j.jnnfm.2011.03.004

Shamekhi, A., & Sadeghy, K. (2009). Cavity flow simulation of Carreau-Yasuda non-Newtonian fluids using PIM meshfree method. *Applied Mathematical Modelling 33,* 4131-4145. https://doi.org/10.1016/j.apm.2009.02.009

Sousa, R. G., Poole, R. J., Afonso, A. M., Pinho, F. T., Oliveira, P. J., Morozov, A., &. Alves, M. A. (2016). Lid-driven cavity flow of viscoelastic liquids. *Journal of Non-Newtonian Fluid Mechanics, 234*, 129-138. https://doi.org/10.1016/j.jnnfm.2016.03.001

Sriram, S., Deshpande, A. P., & Pushpavanam, S. (2008). Characterization of viscoelastic fluid flow in a periodically driven cavity: flow structure, frequency response and phase lag. *Polymer Engineering Science,* 1693-1705. https://doi.org/10.1002/pen.21175

Sun, K.H., Pyle, D. L., Baines, M. J., Hall-Tayler, N., & Fitt, A. D. (2006). Velocity profiles and frictional pressure drop for shear thinning materials in lid-driven cavities with fully developed axial flow. *Chemical Engineering Science, 61*, 4697-4706. https://doi.org/10.1016/j.ces.2006.03.005

Syrakos, A., Georgiou, G. C. A., & Alexandrou, N. (2013). Solution of the square lid-driven cavity flow of a Bingham plastic using the finite volume method. *Journal of Non-Newtonian Fluid Mechanics, 195*, 19-31. https://doi.org/10.1016/j.jnnfm.2012.12.008

Thohura, S., Molla, M., & Sarker, M. M. A. (2019). Bingham fluid flow simulation in a lid-driven skewed cavity using the finite-volume method. *International Journal of Computer Mathematics* https://doi.org/10.1080/00207160.2019.1613527.

Varchanis, S., Syrakos, A., Dimakopoulos, Y., & Tsamopoulos, J. (2019). A new finite element formulation for viscoelastic flows: circumventing simultaneously the LBB condition and the high-Weissenberg number problem. *Journal of Non-Newtonian Fluid Mechanics, 267*, 78-97. https://doi.org/10.1016/j.jnnfm.2019.04.003

Wang, Y., Shu, C., Yang, L. M., & Yuan, H. Z. A(2016). Decoupling multiple-relaxation-time lattice Boltzmann flux solver for non-Newtonian power-law fluids. *Journal of Non-Newtonian Fluid Mechanics, 235*, 20-28. https://doi.org/10.1016/j.jnnfm.2016.03.010

Xu, B., He, L., Wang, M., & Turng, L. S., (2009). Effect of longitudinal periodic length on chaotic mixing in a lid-driven cavity flow system. *Journal of Non-Newtonian Fluid Mechanics, 261,* 81-98. https://doi.org/10.1016/j.jnnfm.2018.08.009

Yesilata, B., Oztekin, A., & Neti, S. (1999). Instabilities in viscoelastic flow through an axisymmetric sudden contraction. *Journal of Non-Newtonian Fluid Mechanics, 85*, 35-62. https://doi.org/10.1016/S0377-0257(98)00183-9

Zhang, J. (2010). An augmented Lagrangian approach to Bingham fluid flows in a lid-driven square cavity with piecewise linear equal-order finite elements. *Computer Methods in Applied Mechanics and Engineering 199*, 3051-3057. https://doi.org/10.1016/j.cma.2010.06.020